Converging super-elliptic torsional shear waves in a bounded transverse isotropic viscoelastic material with nonhomogeneous outer boundary

Martina Guidetti, Diego Caratelli and Thomas J. Royston

Citation: The Journal of the Acoustical Society of America **146**, EL451 (2019); doi: 10.1121/1.5134657
View online: https://doi.org/10.1121/1.5134657
View Table of Contents: https://asa.scitation.org/toc/jas/146/5
Published by the Acoustical Society of America

Converging super-elliptic torsional shear waves in a bounded transverse isotropic viscoelastic material with nonhomogeneous outer boundary

Martina Guidetti,[1] Diego Caratelli,[2,a)] and Thomas J. Royston[1,b)]
[1]*Richard and Loan Hill Department of Bioengineering, University of Illinois at Chicago, 851 South Morgan Street, MC 063, Chicago, Illinois 60607, USA*
[2]*The Antenna Company, High Tech Campus 41, 5656 AE, Eindhoven, The Netherlands*
mguide2@uic.edu, d.caratelli@live.nl, troyston@uic.edu

Abstract: A theoretical approach was recently introduced [Guidetti and Royston, J. Acoust. Soc. Am. **144**, 2312–2323 (2018)] for the radially converging slow shear wave pattern in transverse isotropic materials subjected to axisymmetric excitation normal to the axis of isotropy at the outer boundary of the material. This approach is enabled via transformation to an elliptic coordinate system with isotropic properties. The approach is extended to converging fast shear waves driven by axisymmetric torsional motion polarized in a plane containing the axis of isotropy. The approach involves transformation to a super-elliptic shape with isotropic properties and use of a numerically efficient boundary value approximation.

[JT]
Date Received: September 13, 2019 **Date Accepted:** October 28, 2019

1. Introduction

Please refer to the authors' recent publication in this journal[1] for an extensive summary of the background and motivation for the coordinate transformation strategy extended in the present article to the case of a torsionally-driven radially converging fast shear wave front caused by oscillatory twisting motion of the outer cylindrical boundary. Torsional excitation in this manner could provide an additional efficient means of assessing transversely isotropic material properties, especially if the same cylindrical container could be oscillated independently in axial and torsional directions to drive slow and fast shear waves, respectively, in the same sample. Torsional wave excitation has been explored in applications of ultrasound-based elastography.[2]

Continuous torsional oscillatory motion of a cylindrical boundary normal to its axis generates converging angularly-polarized shear waves that can establish a standing wave pattern in the bounded cylindrical region. While a theoretical solution for the axisymmetric torsional shear wave pattern that is established in isotropic materials is easily obtained using Bessel functions,[3] a solution for the case of anisotropic materials that will produce a nonaxisymmetric shear wave pattern is not as easily found. The configuration considered should result in the generation of only fast shear waves whose phase propagation speed will depend on the angle their direction of propagation makes with the axis of isotropy.

An efficient numerical approach is proposed for the super-elliptic shear wave pattern observed in transverse isotropic materials subjected to axisymmetric excitation parallel to a plane containing the axis of isotropy. The calculated solutions are validated via numerical finite element analysis (FEA) case studies. The numerical approach is also validated via comparison to FEA for the slow shear wave case introduced in Ref. 1.

2. Theory

Please refer to Sec. II A of Ref. 1 for an introduction to the nomenclature and equations used for nearly incompressible isotropic linear viscoelastic material, and for an orientation to the geometry considered in this study. In the present study the outer boundary at $r = r_0$ is oscillated either in the vertical (z) direction as in Ref. 1 or in the torsional (θ) direction as shown in Fig. 1. In the case of transverse isotropy with the y axis parallel to the axis of isotropy (along the fiber axis), axisymmetry (no dependence on θ) in either case is destroyed.

[a)]Also at Eindhoven University of Technology, PO Box 513, 5600 MB, Eindhoven, The Netherlands.
[b)]Author to whom correspondence should be addressed.

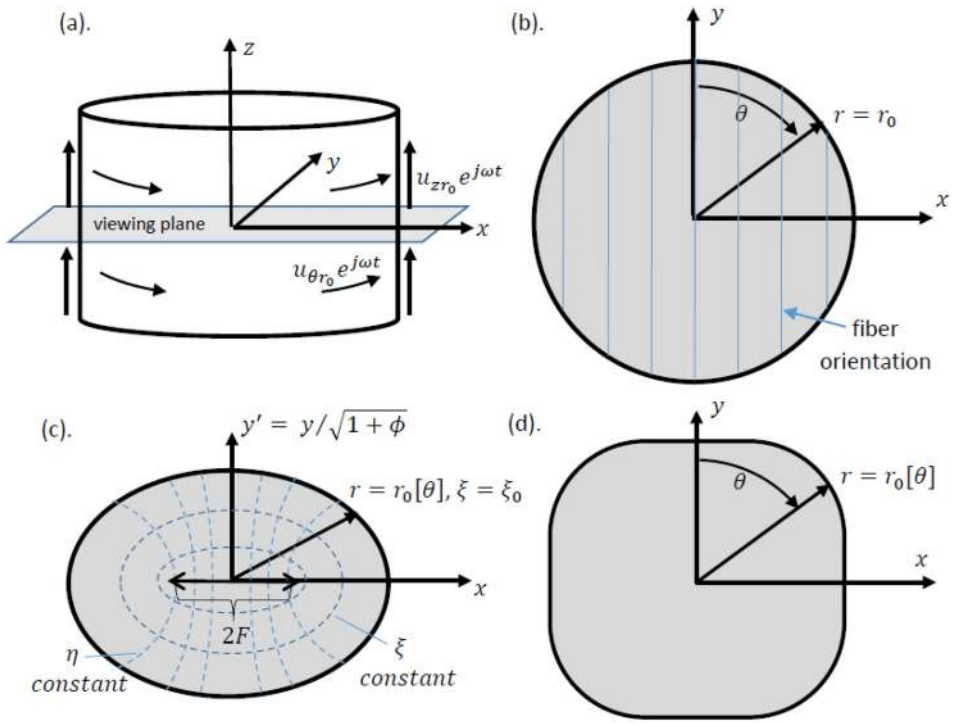

Fig. 1. (Color online) Transverse isotropic cylindrical sample with the x-z plane of isotropy (fibers in the y direction) subjected to a nonhomogeneous boundary condition: harmonic displacement in the $\# \equiv z$ or θ direction of amplitude $u_{\#_{r_0}}$ at frequency $f = \omega/2\pi$ on its curved cylindrical outer boundary at $r = r_o$: (a) system diagram; (b) viewed in the x-y plane; (c) after elliptic transformation for isotropic representation of slow shear waves; and (d) after super-elliptic transformation for isotropic representation of fast shear waves.

Shear wave motion propagating in the r, θ plane with polarization in the z direction, parallel to the plane of isotropy, will have a direction-dependent phase speed c_s given by[4]

$$c_s^2 = \frac{\mu_\perp}{\rho}\left(1 + \phi\cos^2[\theta]\right). \tag{1}$$

The subscript s denotes that this is the "slow" shear wave. The terms $\mu_\perp$, ρ, and ϕ denote the shear elasticity perpendicular to the axis of isotropy (fiber direction), the material density, and the shear anisotropy ($\phi = \mu_{||R}/\mu_{\perp R} - 1$). And here, $\mu_{||R}$ denotes the shear elasticity parallel to the axis of isotropy, with subscript R indicating this is the real part.

Now consider a transformation to a new coordinate system created by distorting distance in a directionally dependent way such that c_s is no longer dependent on direction of propagation: $c_s^2 = \mu_\perp/\rho$. In other words, the material presents itself as isotropic. In the new coordinate system, what was a distance r from the origin is now given by

$$r[\theta] = r/\left(1 + \phi\cos^2[\theta]\right). \tag{2}$$

This transforms what was a circle of radius r into an ellipse as shown in Fig. 1(c). Note, this transformation is what will be used for a purely elastic case or for the case that the ratio of shear loss to storage moduli are the same in parallel and perpendicular directions: $\eta_\mu = \mu_{\perp I}/\mu_{\perp R} = \mu_{||I}/\mu_{||R}$. Here, subscripts R and I denote the real and imaginary parts, respectively, of the complex-valued shear moduli. For the more general viscoelastic case when these ratios are not the same, the distortion can be adjusted accordingly so that slow shear waves propagate at the same speed in any direction on the r, θ plane of the new coordinate system.

Shear wave motion propagating in the r, θ plane with polarization in the r, θ plane will have a direction-dependent phase speed c_f given by[4]

$$c_f^2 = \frac{\mu_\perp}{\rho}\left(1 + \phi\cos^2[2\theta] + \zeta\sin^2[2\theta]\right). \tag{3}$$

The subscript f denotes that this is the "fast" shear wave. The term ζ denotes the tensile anisotropy ($\zeta = E_{||}/E_\perp - 1$). And here, $E_{||}$ and $E_\perp$ denote the Young's modulus parallel and perpendicular to the axis of isotropy, respectively. Note also that[5] $E_{||} = \mu_\perp(4\zeta + 3)$; thus, there are only three independent elasticity parameters.

Now consider a transformation to a new coordinate system created by distorting distance in a directionally dependent way such that c_f is no longer dependent on direction of propagation: $c_f^2 = \mu_\perp/\rho$. In other words, the material presents itself as isotropic. In the new coordinate system, what was a distance r from the origin is now given by

$$r[\theta] = r/\left(1 + \phi\cos^2[2\theta] + \zeta\sin^2[2\theta]\right). \tag{4}$$

This transforms what was a circle of radius r into a super-ellipse as shown in Fig. 1(d). Note, this transformation is what will be used for a purely elastic case or for the case that the ratio of shear and Young's loss to storage moduli are the same in parallel and perpendicular directions: $\eta_\mu = \mu_{\perp I}/\mu_{\perp R} = \mu_{||I}/\mu_{||R}$ and $\eta_E = E_{\perp I}/E_{\perp R} = E_{||I}/E_{||R}$. For the more general viscoelastic case when these ratios are not the same, the distortion will be adjusted accordingly so that fast shear waves propagate at the same speed in any direction on the r, θ plane of the new coordinate system.

Under isotropic and steady state harmonic conditions, shear wave motion propagating in the r, θ plane, regardless of polarization, can be expressed as $u_\#[r, \theta, t] = u_\#[r, \theta]e^{j\omega t}$, where $\# \equiv z \, or \, \theta$ denotes the polarization direction. Consider the inhomogeneous boundary condition of $u_\#[r = r_0[\theta], \theta] = u_{\#R}$, where $u_{\#R}$ is a non-zero constant.

For the case that $\# \equiv z$ and taking $r_0[\theta] = r_0$, a constant or in other words a circular domain, the exact solution is as follows:

$$u_z[r, t] = u_{zr_0}\frac{J_0[k_s r]}{J_0[k_s r_0]}e^{j\omega t}. \tag{5}$$

Here, $k_s = \omega/c_s$ is the slow shear wave number and J_m is the mth order Bessel function of the first kind. Now consider that $r_0[\theta]$ is not a constant, though is continuous on $0 < \theta < 2\pi$ with $r_0[0] = r_0[2\pi]$. A solution for this boundary value problem can be expressed as follows utilizing the convergence property of the Fourier series:[6,7]

$$u_z[r, t] = \sum_{m=0}^{\infty} J_m[k_s r]\left(A_m\cos[m\theta] + B_m\sin[m\theta]\right)e^{j\omega t}, \tag{6}$$

with

$$\sum_{m=0}^{\infty}\begin{Bmatrix} \boldsymbol{X}^+_{\boldsymbol{n,m}} & \boldsymbol{Y}^+_{\boldsymbol{n,m}} \\ \boldsymbol{X}^-_{\boldsymbol{n,m}} & \boldsymbol{Y}^-_{\boldsymbol{n,m}} \end{Bmatrix}\begin{Bmatrix} \boldsymbol{A_m} \\ \boldsymbol{B_m} \end{Bmatrix} = u_{zr_0}\begin{Bmatrix} \boldsymbol{\delta_{n,0}} \\ \boldsymbol{0} \end{Bmatrix}, \tag{7}$$

where

$$X^\pm_{n,m} = \frac{\epsilon_n}{2\pi}\int_0^{2\pi} J_m\left[k_s r_0[\theta]\right]\cos[m\theta]\begin{Bmatrix} \cos[n\theta] \\ \sin[n\theta] \end{Bmatrix}d\theta, \tag{8}$$

$$Y^\pm_{n,m} = \frac{\epsilon_n}{2\pi}\int_0^{2\pi} J_m\left[k_s r_0[\theta]\right]\sin[m\theta]\begin{Bmatrix} \cos[n\theta] \\ \sin[n\theta] \end{Bmatrix}d\theta. \tag{9}$$

Here $\delta_{n,m}$ denotes the Kronecker delta and ϵ_n denotes the Neumann's symbol, equaling 1 if $n = 0$ or 2 if $n \neq 0$. From the convergence property of Fourier series, we know that the values of the coefficients in Eq. (6) will decrease with increasing m and an approximate solution can be obtained by truncating the summation at some $m = M$. If $r_0[\theta] = r_0/(1 + \phi\cos^2[\theta])$ then $\boldsymbol{B_m} = 0$ and terms in $\boldsymbol{A_m}$ will be nonzero only for even values of m.

Now consider $\# \equiv \theta$ and take $r_0[\theta] = r_0$, a constant or, in other words, a circular domain. The exact solution is as follows, where $'$ denotes $\partial/\partial r$,[3]

$$u_\theta[r, t] = u_{\theta r_\theta}\frac{J_0'[k_f r]}{J_0'[k_f r_0]}e^{j\omega t} = u_{\theta r_\theta}\frac{J_1[k_f r]}{J_1[k_f r_0]}e^{j\omega t}. \tag{10}$$

Here $k_f = \omega/c_f$ is the fast shear wave number. This solution follows from the condition of axisymmetry established by the isotropic, homogeneous medium with symmetric (nonzero at r_0) boundary condition, thus eliminating the first derivatives of higher order Bessel functions that will have θ dependence.

Now consider that $r_0[\theta]$ is not constant, though is continuous on $0 < \theta < 2\pi$ with $r_0[0] = r_0[2\pi]$. A complication that arises with θ polarization of the shear wave is that, unlike in the case of z polarization, the imposed displacement on the outer boundary is no longer tangential to the outer boundary surface. This will lead to some error in the solution that will increase as the variation of $r_0[\theta]$ with respect to θ increases. Acknowledging this source of error, we *approximate* the solution as follows:

$$u_\theta[r,t] \approx \sum_{m=0}^{\infty} J'_m[k_s r]\left(A_m \cos[m\theta] + B_m \sin[m\theta]\right)e^{j\omega t}, \tag{11}$$

with

$$\sum_{m=0}^{\infty}\begin{Bmatrix} \boldsymbol{X}^{+}_{\boldsymbol{n,m}} & \boldsymbol{Y}^{+}_{\boldsymbol{n,m}} \\ \boldsymbol{X}^{-}_{\boldsymbol{n,m}} & \boldsymbol{Y}^{-}_{\boldsymbol{n,m}} \end{Bmatrix}\begin{Bmatrix} \boldsymbol{A_m} \\ \boldsymbol{B_m} \end{Bmatrix} = u_{\theta r_0}\begin{Bmatrix} \boldsymbol{\delta_{n,0}} \\ \boldsymbol{0} \end{Bmatrix}, \tag{12}$$

where

$$X^{\pm}_{n,m} = \frac{\epsilon_n}{2\pi}\int_0^{2\pi} J'_m\left[k_s r_0[\theta]\right]\cos[m\theta]\begin{Bmatrix} \cos[n\theta] \\ \sin[n\theta] \end{Bmatrix} d\theta, \tag{13}$$

$$Y^{\pm}_{n,m} = \frac{\epsilon_n}{2\pi}\int_0^{2\pi} J'_m\left[k_s r_0[\theta]\right]\sin[m\theta]\begin{Bmatrix} \cos[n\theta] \\ \sin[n\theta] \end{Bmatrix} d\theta. \tag{14}$$

Note, $A_1 = B_1 = 0$ since $u_\theta[r=0,t]=0$. And, for $r[\theta] = r/(1+\phi\cos^2[2\theta]+\zeta\sin^2[2\theta])$, values of $\boldsymbol{A_m}$ and $\boldsymbol{B_m}$ will be nonzero only when $m = 0, 4, 8, \ldots$.

3. Numerical validation case studies

The Fourier-based approach described in Sec. 2 was implemented for specific case studies in MATLAB Version R2019a (Mathworks Inc., Natick, MA). To validate the theoretical approach, predictions from it were compared to those from computational FEA.

The case study configuration is based on an experimental setup used by some groups[8,9] to conduct magnetic resonance elastography on biological tissue and phantom material specimens, utilizing geometrically converging shear wave excitation, as summarized in Ref. 1. Geometry and physiologically-relevant material property values for the cases are provided in Table 1, and are consistent with values used previously.[1]

For the slow shear wave simulation (axial z polarization), a numerical structural solid mechanics finite element (FE) study using harmonic analysis (steady state response equivalent to particular solution in the frequency domain) was conducted using COMSOL Multiphysics Version 5.4 software (COMSOL Inc., Stockholm, Sweden). The automatically meshed cylindrical model (8 mm in diameter and 20 mm in axial height) contained 46 724 vertices, 267 162 quadratic tetrahedral elements (0.004 to 0.4 mm in size), 9152 triangular elements, 328 edge elements, and 8 vertex elements. The minimum and average element qualities were 0.176 and 0.662, respectively. The element volume ratio was 0.0565 and the mesh volume was 1004 mm^3. (Mesh resolution was decided upon when further increases had a negligible effect on the solution.) Typical computation times for the single frequency harmonic analysis were about 30 min using a 64-bit operating system, ×64 based processor, Intel® Xeon® CPU E5-2609 (Intel, Santa Clara, CA) 0 with a clock speed of 2.40 GHz, and 256 GB RAM. For the fast shear wave simulation (circumferential θ polarization), a numerical structural solid mechanics FE study using harmonic analysis was conducted using ANSYS Mechanical APDL 2019 R1 software. The direct mesh-generated cylindrical model (8 mm in diameter and 0.38 mm in axial height) contained 21 504 8-node solid185 brick elements with consistent node spacing less than 0.1 mm. (Mesh resolution was decided upon when further increases had a negligible effect on the solution.) Typical computation times for the single frequency harmonic analysis were about 20 s using a 64-bit operating system, ×64 based processor, Intel® Xeon® CPU I7-8850H with a clock speed of 2.60 GHz, and 32 GB RAM. The Fourier-based numerical approach introduced in Sec. 2 used to calculate the results for both types of polarization presented below took ∼0.25 or ∼0.75 s for slow or fast shear waves, respectively, in MATLAB.

Table 1. Geometrical and material parameter values for case study.

Parameter	Nomenclature	Value(s)
Cylinder outer radius	r_0	4 mm
Shear storage modulus in plane of isotropy	$\mu_{\perp R}$	2.77 kPa
Ratio of shear loss to storage moduli	$\eta = \frac{\mu_{\perp I}}{\mu_{\perp R}} = \frac{\mu_{\|I}}{\mu_{\|R}}$	0.15
Shear anisotropy	ϕ	0.3
Tensile anisotropy	ζ	0
Density	ρ	1000 $\frac{kg}{m^3}$
Frequency	f	1 kHz

In Fig. 2 we see a comparison of the Fourier and FE solutions for z polarization on an axial slice (x-y plane) with the displacement excitation for the material parameter values in Table 1. Specifically, in Figs. 2(a) and 2(b) we see the in and out of phase (with respect to the excitation) Fourier-based responses, respectively. The steady state (harmonic analysis) FE solution, in and out of phase, is shown in Figs. 2(c) and 2(d), respectively.

For the FE model, the slice location is at the mid-height level (10 mm). In Fig. 3, line profiles of the Fourier numerical and FE solutions within the slice in Fig. 2 and along the x and y axes, in and out of phase, are plotted to provide a more direct comparison of the complete theoretical and numerical FE results. The percent difference along the x or y axis, $\Delta_x\%$ or $\Delta_y\%$, between theoretical and FE solutions is calculated for plots shown in Fig. 3 by taking the mean of the absolute values of the differences in the displacement profiles divided by the root-mean-square of the theoretical displacement profile.[1] These percent differences are provided in the figure captions.

In Fig. 4 we see a comparison of the Fourier and FE solutions for θ polarization on an axial slice (x-y plane) with the displacement excitation for the material parameter values in Table 1. Specifically, in Figs. 4(a) and 4(b) we see the Fourier-based in and out of phase (with respect to the excitation) responses, respectively. The steady state (harmonic analysis) FE solution, in and out of phase, is shown in Figs. 4(c) and 4(d), respectively.

For the FE model the slice location is at the mid-height level (0.19 mm). In Fig. 5 line profiles of the Fourier numerical and FE solutions within the slice in Fig. 4 and along the $y\,(\theta = 0\,^\circ)$ and $x = y$ $(\theta = 45\,^\circ)$ axes, in and out of phase, are plotted to provide a more direct comparison of the complete theoretical and numerical FE results. The percent difference along the y or x-y axis, $\Delta_y\%$ or $\Delta_{xy}\%$, between theoretical and FE solutions is calculated for plots shown in Fig. 4 by taking the mean of the absolute values of the differences in the displacement profiles divided by the root-mean-square of the theoretical displacement profile.[1] These percent differences are provided in the figure captions.

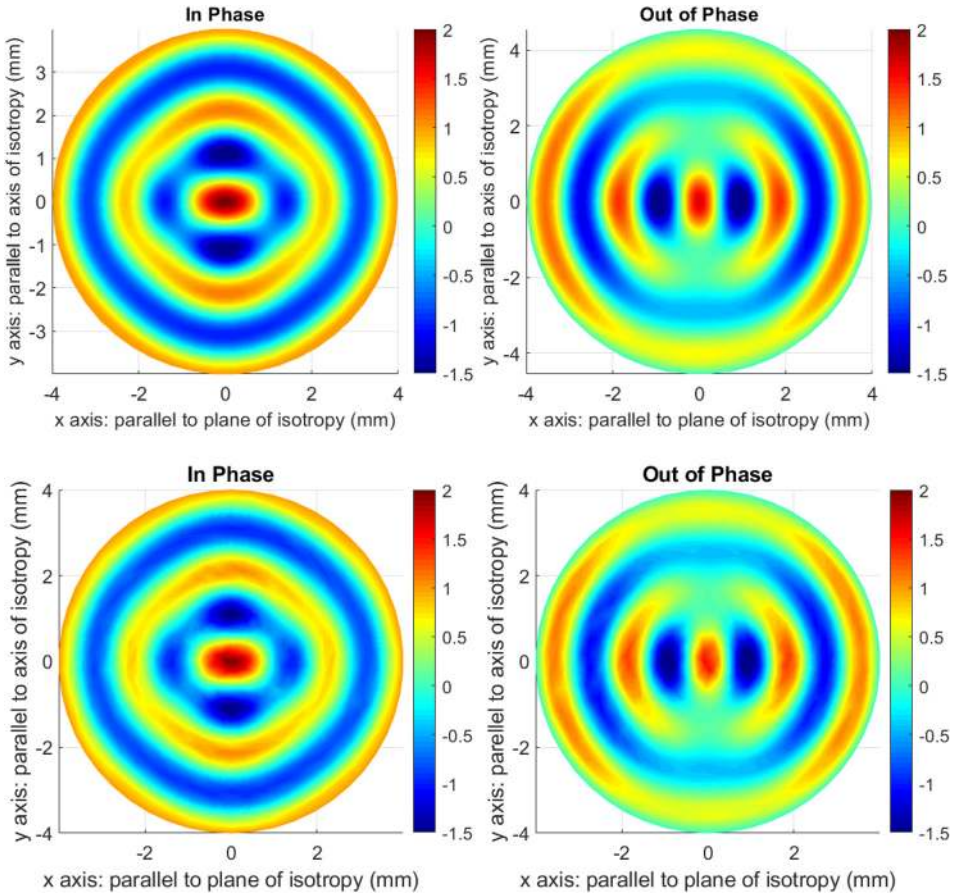

Fig. 2. (Color online) Normalized z direction displacement (u_{zr}/u_{zr_0}) on the x-y plane for z-polarized slow shear waves using the Fourier numerical method [(a) in phase, (b) out of phase] and the FE model [(c) in phase, (d) out of phase]. (See Ref. 10 supplementary material for animations of the Fourier-based numerical solution and FEA solution, respectively, through a complete phase cycle.)

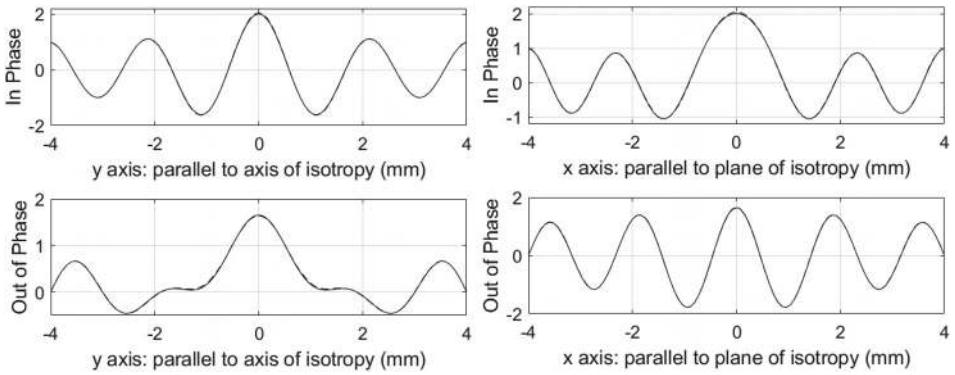

Fig. 3. Normalized z direction displacement (u_{zr}/u_{zr_0}) for z-polarized slow shear waves using the Fourier-based numerical method (solid line) and the FE model (dashed line): (a) along the y (fiber) axis in phase: $\Delta_y = 1.10\%$; (b) along the y (fiber) axis out of phase: $\Delta_y = 1.59\%$; (c) along the x axis in phase: $\Delta_x = 1.43\%$; (d) along the x axis out of phase: $\Delta_x = 0.87\%$.

4. Discussion

In all cases, there is expected to be some small level of error in the numerical FE simulation; it is an approximation. Additionally, neglecting the effect of finite boundaries on the top and bottom of the cylindrical phantom introduces a small amount of error into the theoretical solution for z polarization. Both of these sources of error are thought to be independent of anisotropy. To quantify the combined effect of error in both the FE and theoretical approach independent of anisotropy, the case studies of Sec. III but with $\phi = 0$ (isotropic case) were conducted. Percent differences between the FE and theoretical solutions were calculated the same way. Percent differences, in and out of phase for z polarization, were less than 2.5%, and for θ polarization less than 0.9% and 9.0%, in

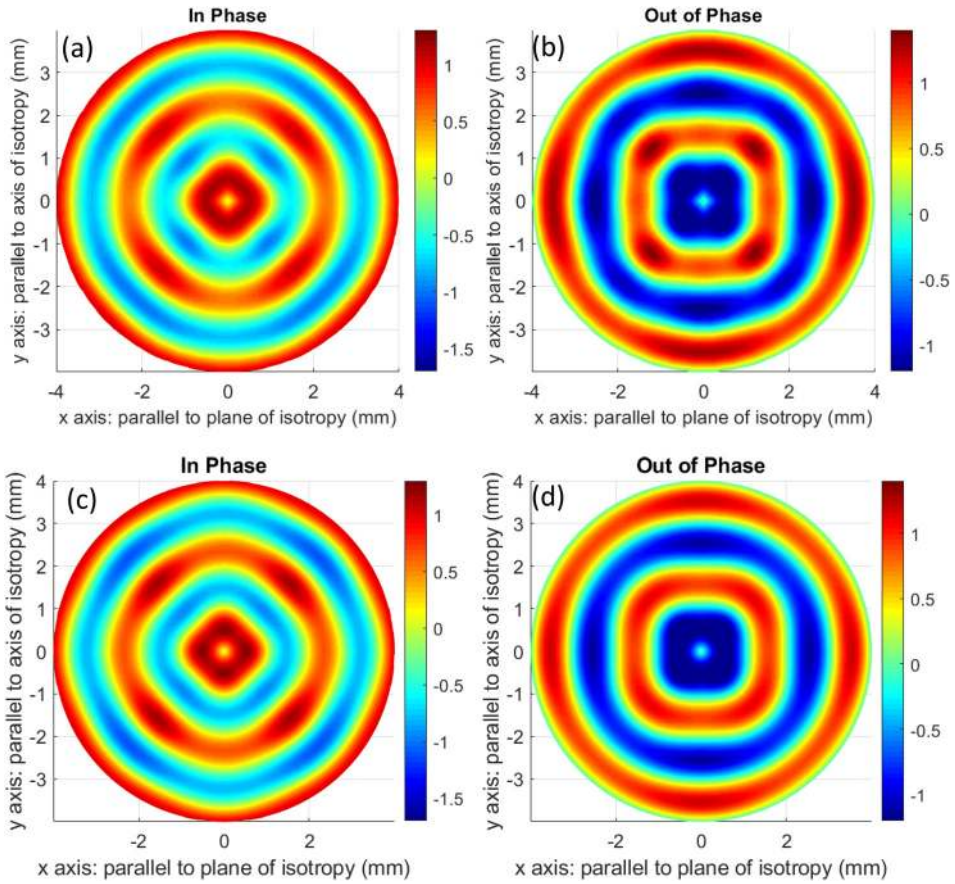

Fig. 4. (Color online) Normalized θ direction displacement $(u_{\theta r}/u_{\theta r_0})$ on the x-y plane for θ-polarized fast shear waves using the Fourier-based numerical method [(a) in phase, (b) out of phase] and the FE model [(c) in phase, (d) out of phase]. (See Ref. 10 for animations of the Fourier-based numerical solution and FEA solution, respectively, through a complete phase cycle.)

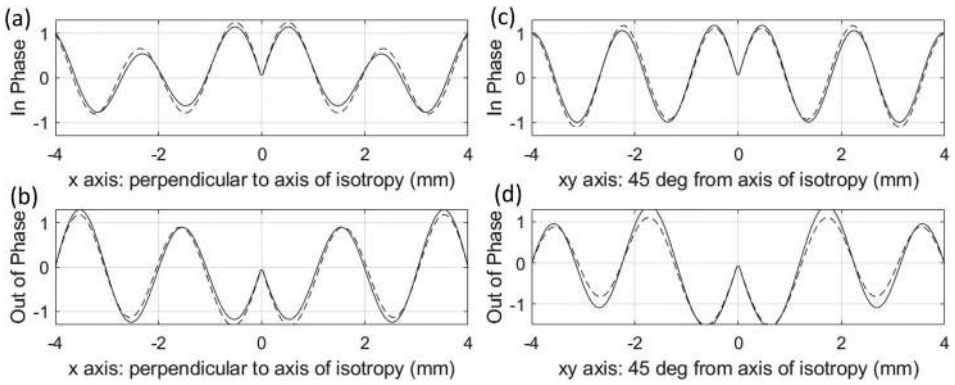

Fig. 5. Normalized θ direction displacement $(u_{\theta r}/u_{\theta r_0})$ for θ-polarized fast shear waves using the Fourier-based numerical method (solid line) and the FE model (dashed line): (a) along the y (fiber) axis in phase: $\Delta_y = 15.5\%$; (b) along the y (fiber) axis out of phase: $\Delta_y = 11.6\%$; (c) along the x-y axis ($\theta = 45°$) in phase: $\Delta_{xy} = 10.4\%$; (d) along the x-y axis out of phase: $\Delta_{xy} = 14.0\%$.

phase and out of phase, respectively, providing target limits for accuracy in the anisotropic cases.

For the anisotropic case with $\phi = 0.3$, the z polarization percent differences (Fig. 3) were all less than 1.6%. Thus, in this case, the Fourier-based approach yields a solution with accuracy that is at least within the limits of precision of the numerical (FE) approach. For θ polarization, percent differences (Fig. 5) ranged from 10.4% to 15.5% and thus exceeded differences found in the isotropic case. This suggests a measurable error in the Fourier-based approach. It is hypothesized that the source of this error is mainly due to the fact that, as the geometry is distorted, the θ-polarized displacement input at the outer curved boundary is no longer perfectly tangential to that boundary at all values of θ. This is a distinct difference from the z polarization, which is always tangent to the outer curved boundary no matter the level of distortion (variation of outer radius R as a function of θ). Increasing differences between FEA and the Fourier-based approach with increased values of ϕ (four error values reported in Fig. 5 averaging to 5.1%, 12.9%, and 39.0% for $\phi = 0.1$, 0.3, and 1.0, respectively) support this hypothesis and highlight a limitation of the Fourier-based approach.

Acknowledgments

M.G. and T.J.R. acknowledge funding from NSF Grant No. 1852691 and NIH Grant No. AR071162.

References and links

[1]M. Guidetti and T. J. Royston, "Analytical solution for converging elliptic shear wave in a bounded transverse isotropic viscoelastic material with nonhomogeneous outer boundary," J. Acoust. Soc. Am. **144**, 2312–2323 (2018).

[2]J. Melchor, R. Muñoz, and G. Rus, "Torsional ultrasound sensor optimization for soft tissue characterization," Sensors **17**, 1402 (2017).

[3]K. Graff, *Wave Motion in Elastic Solids* (Dover, New York, 1991).

[4]D. J. Tweten, R. J. Okamoto, J. L. Schmidt, J. R. Garbow, and P. V. Bayly, "Estimation of material parameters from slow and fast shear waves in an incompressible, transversely isotropic material," J. Biomech. **48**, 4002–4009 (2015).

[5]J. L. Schmidt, D. J. Tweten, A. N. Benegal, C. H. Walker, T. E. Portnoi, R. J. Okamoto, J. R. Garbow, and P. V. Bayly, "Magnetic resonance elastography of slow and fast shear waves illuminates differences in shear and tensile moduli in anisotropic tissue," J. Biomech. **49**, 1042–1049 (2016).

[6]D. Caratelli, P. Natalini, and P. E. Ricci, "Fourier solution of the wave equation for a star-like-shaped vibrating membrane," Comp. Math. Appl. **59**, 176–184 (2010).

[7]D. Caratelli, J. Gielis, I. Tavkhelidze, and P. E. Ricci, "Fourier-Hankel solution of the Robin problem for the Helmholtz equation in supershaped annular domains," Bound. Value Probl. **253**, 1–11 (2013).

[8]T. K. Yasar, T. J. Royston, and R. L. Magin, "Wideband MR elastography for viscoelasticity model identification," Mag. Res. Med. **70**, 479–489 (2013).

[9]J. Braun, H. Tzschatzsch, C. Korting, A. A. de Schellenberger, M. Jenderka, T. Driessle, M. Ledwig, and I. Sack, "A compact 0.5 T MR elastography device and its application for studying viscoelasticity changes in biological tissues during progressive formalin fixation," Magn. Reson. Med. **79**, 470–478 (2018).

[10]See supplementary material at http://dx.doi.org/10.1121/1.5134657 for animations of the Fourier-based numerical solution and FEA solution, respectively, through a complete phase cycle.